Nanoelectronics and Its New Materials – A NEW ERA OF NANOSCIENCE

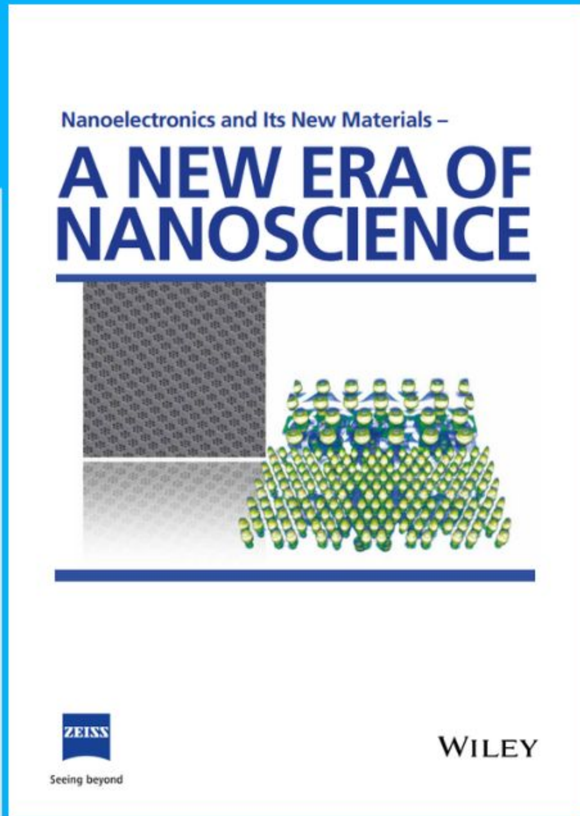

Discover the recent advances in electronics research and fundamental nanoscience.

Nanotechnology has become the driving force behind breakthroughs in engineering, materials science, physics, chemistry, and biological sciences. In this compendium, we delve into a wide range of novel applications that highlight recent advances in electronics research and fundamental nanoscience. From surface analysis and defect detection to tailored optical functionality and transparent nanowire electrodes, this eBook covers key topics that will revolutionize the future of electronics.

To get your hands on this valuable resource and unleash the power of nanotechnology, simply download the eBook now. Stay ahead of the curve and embrace the future of electronics with nanoscience as your guide.

Seeing beyond

WILEY

ADVANCED FUNCTIONAL MATERIALS
www.afm-journal.de

Check for updates

Confocal Microscopy for In Situ Multi-Modal Characterization and Patterning of Laser-Reduced Graphene Oxide

*Yuhan Li and Milo S. P. Shaffer**

Graphene oxide (GO) films can be readily prepared at wafer scale, then reduced to form graphene-based conductive circuits relevant to a range of practical device applications. Among a variety of reduction methods, laser processing has emerged as an important technique for localized reduction and patterning of GO films. In this study, the novel use of confocal microscopy is demonstrated for high-resolution characterization, in situ laser reduction, and versatile patterning of GO films. Multi-modal imaging and real-time tracking are performed with 405 and 488 nm lasers, enabling large-area direct observation of the reduction progress. Using image analysis to cluster flake types, the different stages of reduction can be attributed to thermal transfer and accumulation. Delicate control of the reduction process over multiple length scales is illustrated using millimeter-scale stitched patterns, micro-patterning of single flakes, and direct writing conductive 2D wires with sub-micrometer resolution (530 nm). The general applicability of the technique is shown, allowing fabrication of both conductive reduced graphene oxide (rGO) films (sheet resistance: 2.5 kOhm sq^{-1}) and 3D microscale architectures. This simple and mask-free method provides a valuable tool for well-controlled and scalable fabrication of reduced GO structures using compact low-power lasers (< 5 mW), with simultaneous in situ monitoring and quality control.

1. Introduction

Graphene oxide (GO) has been extensively researched as an inexpensive and scalable precursor material for synthesis of graphene-related structures.[1] The fabrication of thin films on various substrates is particularly well studied, with promising applications in flexible electronics and energy storage devices.[2] In many cases, the GO must be converted into a conductive graphitic material known as reduced graphene oxide (rGO).[3] State-of-the-art reduction processes include thermal, chemical, and microwave treatments.[4] Patterns of reduced (conductive) and unreduced (insulating) GO can provide efficient routes to a variety of devices, including supercapacitors and sensors.[5] The locus of reduction can be controlled using masks, photoresists, or local scanning probe heating.[6] One particularly attractive route is the application of laser irradiation to directly pattern reduced GO, in a single step, without additional chemicals or masks.[7]

Laser reduction of GO is usually achieved using high-power industrial laser setups. As GO is a broadband light absorber, laser reduction has been performed using a variety of sources, with wavelengths ranging from the ultraviolet to the infrared.[8] The wavelength, laser power, and scanning speed, alongside other laser or scanning parameters, have been explored to modulate the reduction process, achieving varying resolutions, degrees of reduction, and electrical performance.[9] Typically, GO films with thicknesses ranging from tens of nanometers to micrometers are deposited by spin coating, drop-casting, filtration, or other techniques, before microscale reduction patterns are created through controlled rastering.[9a,10] Higher pattern resolutions, down to a few micrometers, usually requires shorter wavelength (ultraviolet-green) or pulsed (nanosecond-femtosecond) lasers.[8a,11] Using femtosecond lasers featuring ultrashort pulse width, line resolutions have been reported down to 500 nm.[12] The extent of reduction can be adjusted through the time and power of exposure, which is evidenced after processing by electrical conductivity measurements, or through Raman or X-ray photoelectron spectroscopies.[13] However, a more detailed understanding of the reduction process is needed in order to adjust performance and maintain control in complex geometries. Unfortunately, it is challenging to visualize the reduction process of GO directly, as the films are densely packed and become increasingly opaque as they are reduced, making it difficult to resolve the behavior of individual flakes. Current understanding of the reduction mechanism is generally based on comparisons

Y. Li, M. S. P. Shaffer
Department of Materials
Imperial College London
Exhibition Road, London SW7 2AZ, UK
E-mail: m.shaffer@imperial.ac.uk

M. S. P. Shaffer
Department of Chemistry
Imperial College London
82 Wood Lane, London W12 0BZ, UK

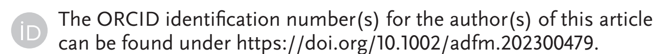
The ORCID identification number(s) for the author(s) of this article can be found under https://doi.org/10.1002/adfm.202300479.

© 2023 The Authors. Advanced Functional Materials published by Wiley-VCH GmbH. This is an open access article under the terms of the Creative Commons Attribution License, which permits use, distribution and reproduction in any medium, provided the original work is properly cited.

DOI: 10.1002/adfm.202300479

 © 2023 The Authors. Advanced Functional Materials published by Wiley-VCH GmbH

16163028, 2023, 30, Downloaded from https://onlinelibrary.wiley.com/doi/10.1002/adfm.202300479 by Imperial College London, Wiley Online Library on [24/08/2023]. See the Terms and Conditions (https://onlinelibrary.wiley.com/terms-and-conditions) on Wiley Online Library for rules of use; OA articles are governed by the applicable Creative Commons License

of microstructural features or chemical compositions of the starting material and final rGO.[14] Single layer GO (flake size: 5-10 μm) reduction was previously observed in situ, using an absorption instrument built on an inverted optical microscope to record absorption/emission maps.[15] A complex series of sequential processes occurred, including the reduction of GO, fragmentation, and then photobleaching of rGO.[15,16] GO films contain a large number of GO flakes of different sizes packed into a heterogenous array; in this case, direct visualization and large-scale tracking of multiple GO flakes are required over a large area to understand how the reduction progresses throughout the material.

Confocal laser scanning microscopy (CLSM) provides a method to realize simultaneous in situ GO reduction and characterization with the built-in laser scanning system. Previously, reflection mode CLSM has been explored as a high contrast tool for real-time monitoring of CVD graphene on copper foil.[17] With advantages of large-scale and high-resolution scanning, confocal microscopy can be extremely useful for rapid imaging and in situ study of graphene and its derivatives.[18] Furthermore, the integration of multiple modules on modern confocal microscope systems enables multi-channel imaging, combining transmission, reflection, and fluorescence modalities. GO exhibits unique photoluminescent properties and light absorption in the ultraviolet and visible range.[19] As GO is reduced to rGO, the change in optical properties manifests as a decrease in fluorescence emission and an increase of both refractive index and extinction coefficient, which contribute to altered image contrast.[11b,20] In this paper, we demonstrate that multi-modal CLSM has great potential for tracking and modulating the laser reduction of GO.

This study investigates the extended applications of CLSM fin situ reduction and real-time monitoring of GO films over large areas. Multiple-pass correlative imaging applying 488 and 405 nm diode lasers is designed to directly visualize the laser reduction process of GO films. The reduction progress is demonstrated with microscopic multimedia captured at various length scales, interpreted quantitatively, assigning flakes to different phenomenological clusters, using image analysis. As well as demonstrating the utility of CLSM methods, the aim of this study was to explore the reduction mechanism and process limits of laser reduced GO films. With the flexibility of CLSM, it is expected that high-resolution reduction patterns can be achieved through the modulation of processing parameters; the concept is demonstrated by patterning across a very broad range of length scales.

2. Results and Discussion

2.1. Multi-Modal Imaging of GO Flakes with Confocal Microscopy

Initially, in order to characterize the responses of individual GO flakes, a diluted GO solution was spin-coated onto glass substrates. Characterization of GO with conventional optical microscopy or scanning electron microscopy (SEM) is challenging as GO has lower optical absorption and much lower electrical conductivity than both ideal graphene and rGO. CLSM offers improved contrast and resolution,[21] and is particularly well-suited to the observation of GO over large areas. The bulk absorbance and reflectance, and fluorescence spectra of the deposited GO films (Figure S2, Supporting Information) show the expected broad interactions with light over the ultraviolet-visible region and highlight the various optical imaging modes available. Correlative multimodal imaging reveals richly detailed information on the GO flake structure and distribution (**Figure 1**). In the transmission-mode optical image, the GO flakes appear darker than the glass substrate due to higher light absorption (Figure 1a), while in the reflection mode image the contrast is inverted (Figure 1b). Compared with conventional transmission imaging, confocal reflection-mode imaging (Figure 1b) provides improved contrast, in which thin-layer flakes are well resolved with excellent resolution. GO has weak broadband fluorescence in the near infrared range due to the reduced extent of conjugation associated with the covalently bound oxygen groups.[22] As a result, a fluorescence signal (565–700 nm) appears in the areas covered by GO (Figure 1c). However, the signal-to-noise ratio of fluorescence imaging is lower than reflection imaging due to the low photoluminescent efficiency (PL quantum yield < 1%).[23] The ambient, high speed, and large area imaging capability of multi-modal CLSM complements existing techniques routinely applied for studying GO.

2.2. In Situ Laser Reduction and Large-Scale Monitoring

Various laser sources have been used to induce the photoreduction of GO; a laser energy threshold (3.2 eV; ≈390 nm) has been proposed between photochemical and photothermal reactions.[24] For laser wavelengths above 390 nm, photothermal reduction is expected to dominate; however, the mechanism

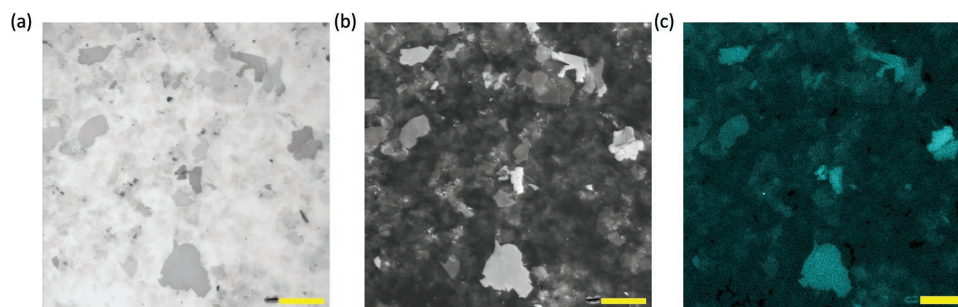

Figure 1. a) Transmission-mode optical image of GO flakes. b) Confocal reflection-mode image (3.4% laser power, maximum projection from a 3D stack). c) Photoluminescence image of the GO film (64% laser power). Scale bar: 20 μm.

© 2023 The Authors. Advanced Functional Materials published by Wiley-VCH GmbH

16163028, 2023, 30, Downloaded from https://onlinelibrary.wiley.com/doi/10.1002/adfm.202300479 by Imperial College London, Wiley Online Library on [24/08/2023]. See the Terms and Conditions (https://onlinelibrary.wiley.com/terms-and-conditions) on Wiley Online Library for rules of use; OA articles are governed by the applicable Creative Commons License

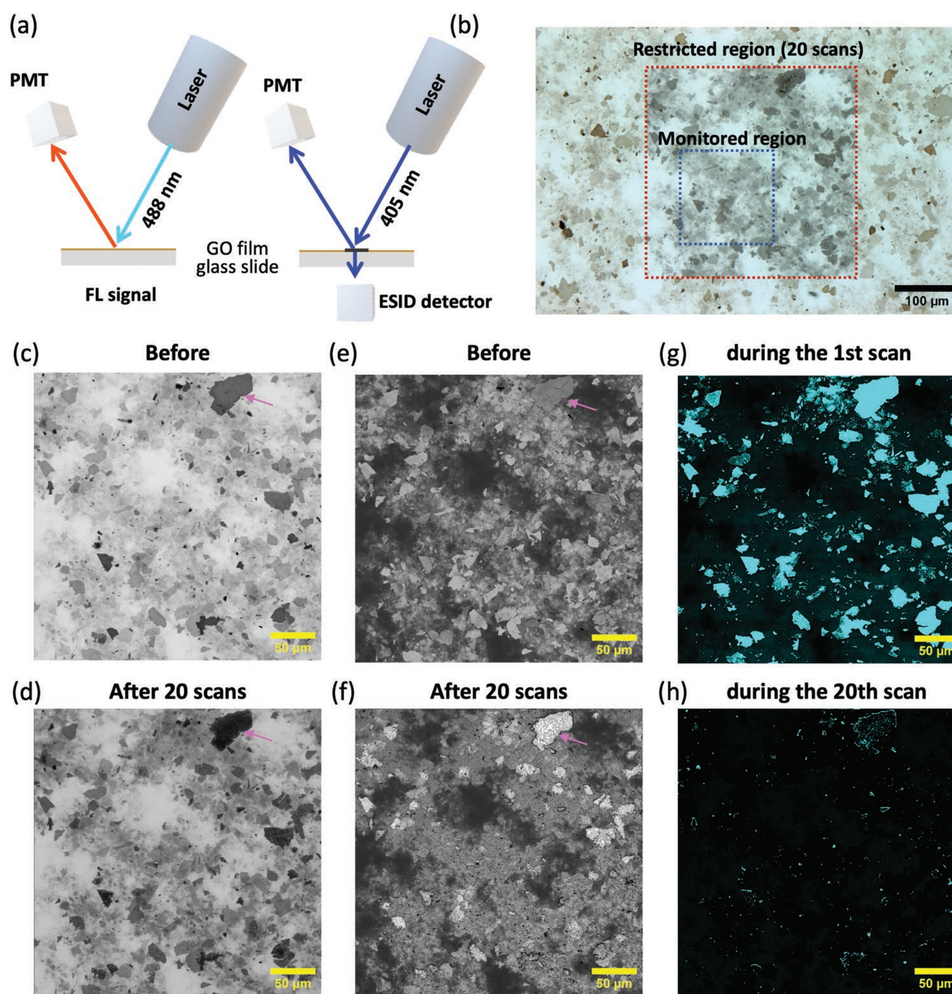

Figure 2. Schematic diagram showing the laser set up for in situ reduction and tracking. b) Widefield optical micrograph of an area reduced with 488 nm laser (20 scans). The red box indicates the laser restricted region, and the blue box indicates the area monitored. c,d) Transmission images. A large GO flake is indicated by pink arrows in c-f highlighting the contrast change. e,f) Confocal reflection images acquired with a 405 nm laser before and after laser reduction. g,h) Fluorescence images taken during the 1st and the 20th reduction.

is complex and poorly understood, involving decomposition, evaporation and material ablation.[8a,25] A multiple-pass imaging setup was, therefore, designed to study the process in more detail (**Figure 2**a): a strong 488 nm laser (80% power) was used first to initiate photoreduction while also generating a measurable photoluminescence signal during the scanning process. The second pass applied a weak 405 nm laser (3.4% power) for high resolution transmission/reflection imaging, which captures the contrast change induced by the first step, without inducing any further structural changes. In a typical experiment, this sequence was applied to a GO film with an area of 319.5 µm × 319.5 µm; the whitelight optical micrograph shows a noticeable color difference between the laser exposed region (dark gray) and the surrounding untreated region (brown) (Figure 2b). Multimodal observation shows the sequential development of distinct optical features and surface structures as GO is transformed into laser reduced GO (LrGO). Most significantly, in the transmission images, the flakes darken following laser processing indicating an increase of optical absorbance (Figure 2c,d). In reflection-mode imaging, the reduction of GO delivers two distinct contributions to the contrast. Improved contrast was observed for some large GO flakes which become brighter in the reflection images, due to the increase in refractive index of LrGO (Figure 2e,f), as was previously reported for thermally reduced GO.[20,26] However, some dark points also appear on the flake surface after processing, which can be attributed to the rougher surface of LrGO causing diffuse reflection (see Figure 2f). During reduction, the fluorescence intensities correspondingly fall monotonically between the 1st and 20th scans (Figure 2g,h). Overall, both transmission and fluorescence images demonstrate the suitability of CLSM imaging for real-time monitoring of the reduction process. Meanwhile, the reflection imaging mode is useful for studying the surface morphology of LrGO flakes and films.

To explore the sequential laser reduction process, the fluorescence signal was monitored over a selected area (**Figure 3**), and the total fluorescence intensity integrated as a function of laser scan number (Figure S3, Supporting Information). The most dramatic drop in photoluminescence was observed between the 1st and 2nd scans, followed by a more gradual decay, until

 © 2023 The Authors. Advanced Functional Materials published by Wiley-VCH GmbH

ADVANCED FUNCTIONAL MATERIALS
www.afm-journal.de

16163028, 2023, 30, Downloaded from https://onlinelibrary.wiley.com/doi/10.1002/adfm.202300479 by Imperial College London, Wiley Online Library on [24/08/2023]. See the Terms and Conditions (https://onlinelibrary.wiley.com/terms-and-conditions) on Wiley Online Library for rules of use; OA articles are governed by the applicable Creative Commons License

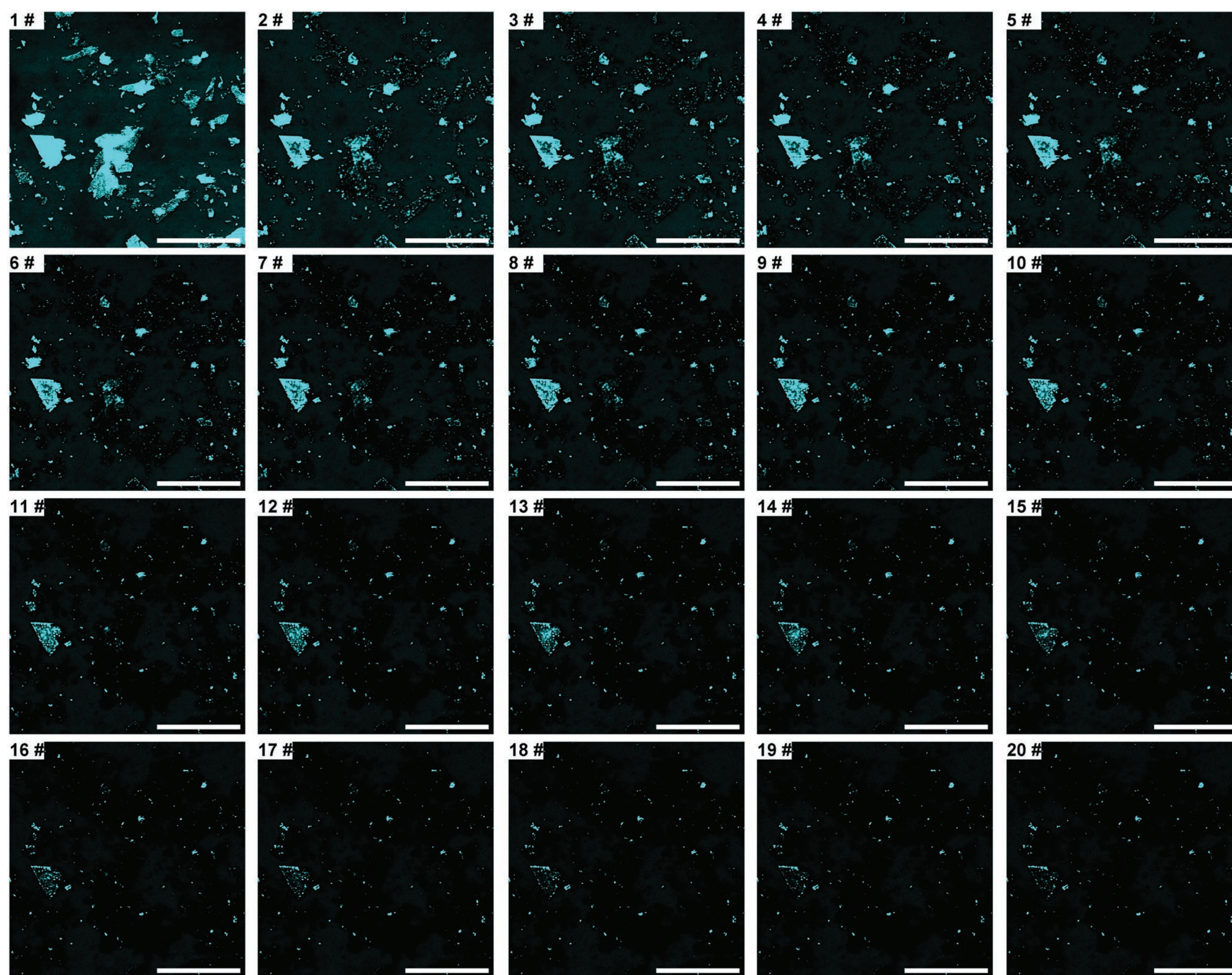

Figure 3. Fluorescence signal from a selected region of GO films during 20 sequential laser reduction scans (scale bar: 50 µm).

most of the signal disappears, with no obvious further change after 18 scans. The persistent fluorescence remaining in the final images can be attributed to the emission from trapped sp^2 domains, associated with defect structures; GO never converts perfectly back to graphite due to the loss of carbon from the framework.[11b,15]

The sequential reduction process was also observed using optical transmission images collected immediately after each laser scan, showing a systematic reduction in both the complete transmission datasets (Video S1, Supporting Information) and periodic snapshots (**Figure 4**a). A quantitative relative pixel conversion degree (see Experimental Section for details) was calculated to allow convenient tracking of the reduction process (Figure 4b). In brief, the relative conversion degree describes the absorbance change in comparison with the total absorbance variation range measured (from the initial GO to the fully reduced product) for each pixel. Correspondingly, the increasing degree of reduction is indicated by a color change from blue (the 1st scan) to light blue (the 5th scan), yellow (the 10th scan) and red (the 20th scan) in the conversion maps. The reduction trajectory follows two different paths depending on the type of GO flake. For the darkest, discrete flakes, immediate reduction is followed by local ablation. Specifically, these flakes (example highlighted by an arrow in (Figure 4a)) show obvious darkening in the transmission image and a very high immediate conversion degree after the 1st scan, but apparently decreasing conversion degree in the subsequent scans. Other regions of thinner GO flakes show a more progressive reduction, including both a locally increasing degree of conversion and gradual extension of the reduced area (see circled region in Figure 4a).

Since this quantification of the reduction progress highlights different phenomenology for different flakes, a more formal classification method was applied. A cluster analysis allows for efficient statistical investigation of flake behavior over a large scale, which is especially beneficial for such a complex system formed by randomly distributed flakes. In this case, a one-step *k*-means algorithm was used to cluster the pixels into different groups according to the optical features of the original transmission image (**Figure 5**a). *K*-means is an unsupervised statistical learning method, which separates datasets based on similar features. This algorithm has been applied to rapid clustering

 © 2023 The Authors. Advanced Functional Materials published by Wiley-VCH GmbH

16163028, 2023, 30, Downloaded from https://onlinelibrary.wiley.com/doi/10.1002/adfm.202300479 by Imperial College London, Wiley Online Library on [24/08/2023]. See the Terms and Conditions (https://onlinelibrary.wiley.com/terms-and-conditions) on Wiley Online Library for rules of use; OA articles are governed by the applicable Creative Commons License

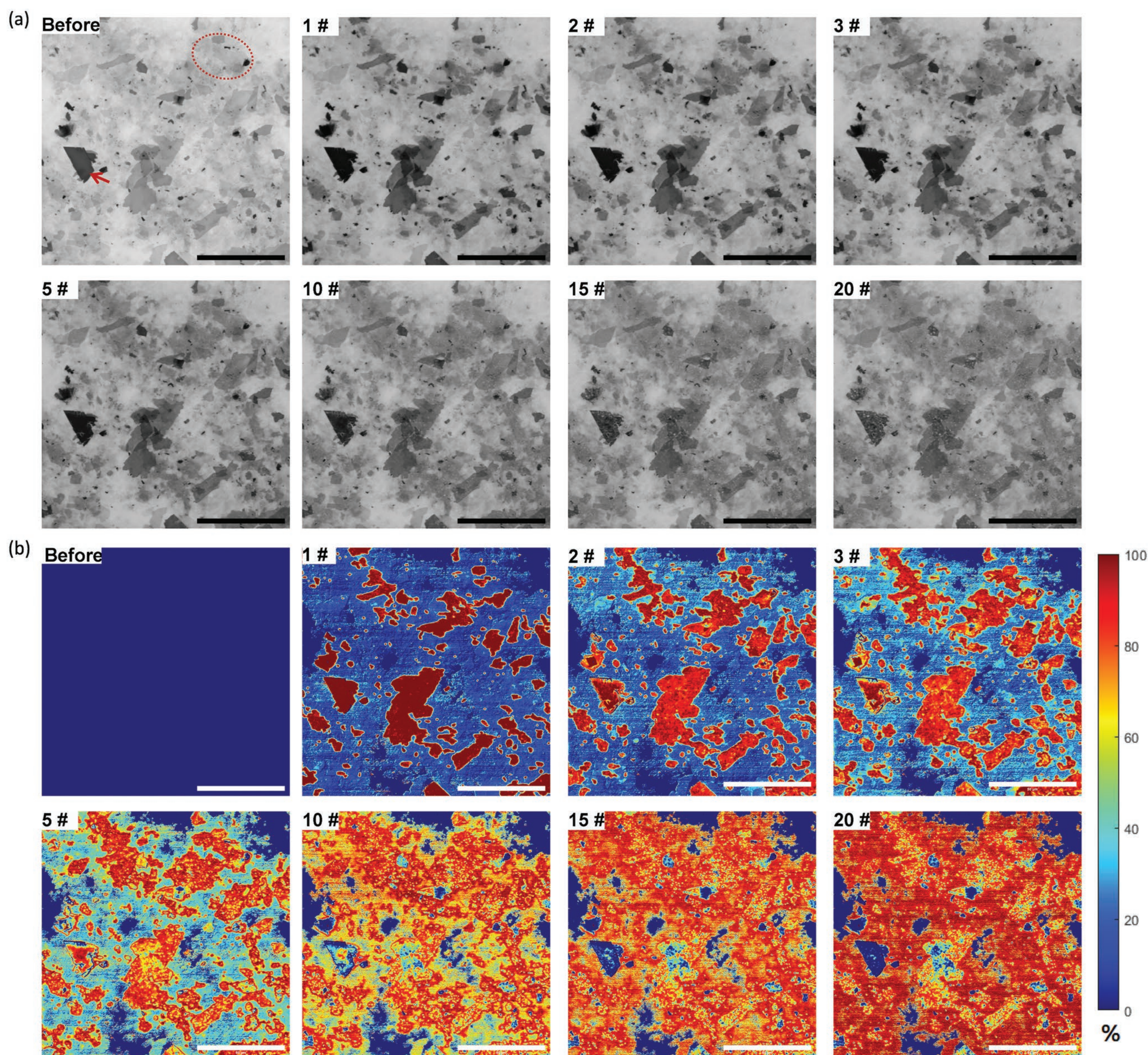

Figure 4. a) Representative transmission-mode images acquired after different numbers of laser reduction scans (first row: before processing, and the 1st–3rd scan. Second row: the 5th, 10th, 15th, and 20th scan). Featured regions are indicated in the first image. b) Corresponding percentage conversion colormaps showing the relative reduction degree calculated from the transmission micrographs in a).

of microscopic image datasets of materials with complex spatial distributions in the literature,[27] and thus was chosen as a suitable clustering method here. Four (k) independent clusters were chosen to group the pixels into areas covered by the glass substrate (cluster 0), thin layers (cluster 1), medium layers (cluster 2), and thick GO flakes (cluster 3), respectively. From the labelled image (Figure 5b), most regions of GO are successfully identified with clear boundaries between the clusters. The clustering is assigned based on the pixel intensity features, which is correlated here with the absorption by GO and hence a statistical classification of flake thicknesses. The linear relationship between layer numbers and optical absorbance was previously used to determine the thickness of graphene,[28] and was adopted here for efficient estimation of flake thicknesses over a large area. Specifically, the optical absorbance of rGO was determined by analyzing normalized pixel intensities in the transmission images. The absorbance values were converted to flake thickness using the extinction coefficient of rGO ($\alpha_{405\ \mathrm{nm}} \approx 21.6 \pm 0.6 \times 10^4\ \mathrm{cm}^{-1}$).[15] Atomic force microscopy (AFM) images of representative GO flakes (Figure S4b–d, Supporting Information) reveal a wide distribution of thicknesses (a few nanometers to tens of nanometers); a full correlative analysis would take significant time and effort. In contrast, optical absorbance provides a convenient method for statistical analysis of thickness distribution across a large region, for each of the 3 different clusters (Figure S4a, Supporting Information).

 © 2023 The Authors. Advanced Functional Materials published by Wiley-VCH GmbH

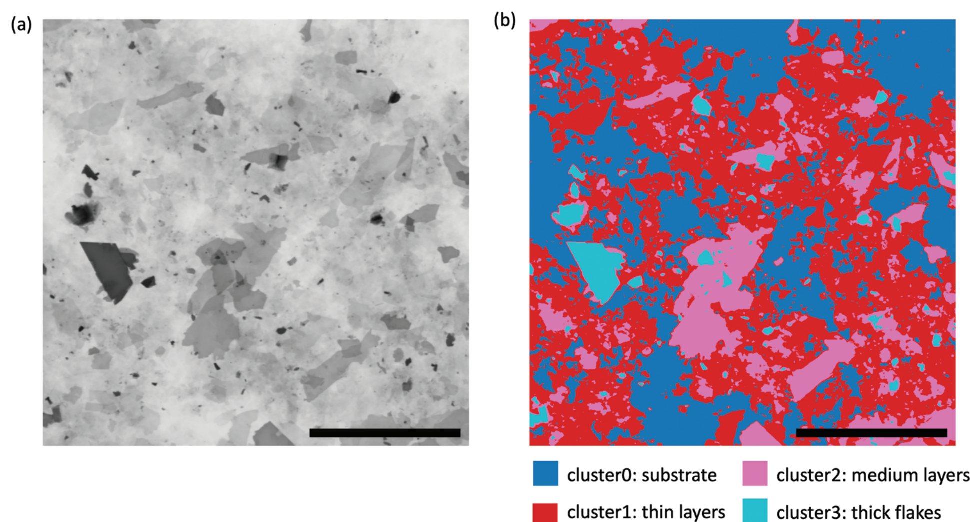

Figure 5. a) Transmission-mode micrograph of GO flakes before processing. b) Color labelled image obtained from a *k*-means clustering method based on the pixel intensity of GO flakes. Scale bar: 50 µm.

Nevertheless, this statistical analysis demonstrates a thickness range consistent with the AFM measurements. Each cluster spans a characteristic thickness range; the thin flake cluster (cluster 1) is relatively well defined with thicknesses of below 12 nm and a narrow, symmetrical distribution. Cluster 2 comprises thicker flakes ranging from 10–24 nm with a broader, positively-skewed distribution. The largest flakes are in cluster 3 which range from ≈20 nm to above 46 nm, with a negatively-skewed distribution. However, more than 85% of GO in cluster 3 has a thickness of >24 nm. The slight overlap between clusters, in particular clusters 2 and 3, can be attributed to less well-defined boundary pixels and overlapping flakes, as well as the nature of the clustering algorithm used. Broadly, the flake clusters are well separated. A multi-panel movie was generated by considering the sequential conversion maps of each of the three GO cluster types independently (Video S2, Supporting Information). For thin GO layers (cluster 1), the real-time tracking confirms a gradual conversion and extension of reduced regions. Both cluster 2 and cluster 3 achieved almost full conversion after the first laser scan, indicating instant reduction in relatively thick GO flakes. In the following scans, the apparently decreasing degree of conversion degree can be attributed to laser ablation removing carbonaceous LrGO material from the image path. The categorization of flake clusters, via automated image analysis, simplifies process tracking and confirms that the reduction process is closely related to the initial thickness of the GO flakes. The qualitative differences between the reduction behavior of thin layers (cluster 1) and thick flakes (cluster 3) are clear; while cluster 2 flakes show a similar reduction progress to cluster 3, they achieve a higher final degree of conversion, and may, therefore, be useful to distinguish.

In order to resolve the initial reduction steps more clearly, laser scans were collected at lower intensities (60% and 40%). For each cluster, the proportion of pixels showing full conversion was plotted as a function of the number of laser scans (Figure S5, Supporting Information), showing that thin-layer GO (cluster 1) and thicker GO (cluster 2 and 3) flakes indeed have significantly different conversion rates. A cumulative distribution was generated to illustrate how the ratio of reduced pixels per cluster varies over increasing laser scans (**Figure 6**). Again, the thickest flakes (cluster 3) convert most quickly, closely followed by medium flakes (cluster 2). In contrast, the most sequential reduction process is observed in the thin layer GO (cluster 1), with an initial reduction rate that decreases as the laser power is reduced. For the 488 nm continuous-wave laser applied for reduction, the photon energy (2.5 eV) is far below the laser energy threshold and photothermal reduction is expected to be the predominant mechanism.[29] As such, the distinct phenomenology can be attributed to thermal transfer and heat accumulation effects during laser exposure (Figure 6d). As the laser irradiates the film, energetic photons are absorbed and heat is generated. In thin GO, thermal energy dissipates efficiently due to the high thermal conductivity of the underlying substrate, leading to a controlled reduction process. In addition, the evolved gases associated with reduction (such as CO, CO_2) easily dissipate.[30] In thick flakes, heating is more rapid due to the greater optical absorbance, and relatively slower dissipation due to the low out of plane thermal conductivity of layered materials.[31] In addition, in thick flakes, the evolved gases can be partly trapped between the layers, leading to expansion (see below), decreasing thermal conductivity substantially. As the reduction proceeds, the material darkens and absorbs more laser energy accelerating the process; due to the thermal isolation from the substrate, this feedback can lead to ablation and hence a porous or fragmented structure.[9b]

2.3. High Magnification Tracking of Single Flake Reduction

Taking advantage of the flexibility of CLSM, the thermal-dominated reduction mechanism was investigated within individual GO flakes. High magnification tracking of two GO flakes representing the conversion of thin layer and thicker flakes (Figure S6, Supporting Information) was achieved by switching to high magnification (500X) in between the reduction sequences (laser power: 40%). Transmission-mode micrographs and associated

© 2023 The Authors. Advanced Functional Materials published by Wiley-VCH GmbH

16163028, 2023, 30, Downloaded from https://onlinelibrary.wiley.com/doi/10.1002/adfm.202300479 by Imperial College London, Wiley Online Library on [24/08/2023]. See the Terms and Conditions (https://onlinelibrary.wiley.com/terms-and-conditions) on Wiley Online Library for rules of use; OA articles are governed by the applicable Creative Commons License

16163028, 2023, 30, Downloaded from https://onlinelibrary.wiley.com/doi/10.1002/adfm.202300479 by Imperial College London, Wiley Online Library on [24/08/2023]. See the Terms and Conditions (https://onlinelibrary.wiley.com/terms-and-conditions) on Wiley Online Library for rules of use; OA articles are governed by the applicable Creative Commons License

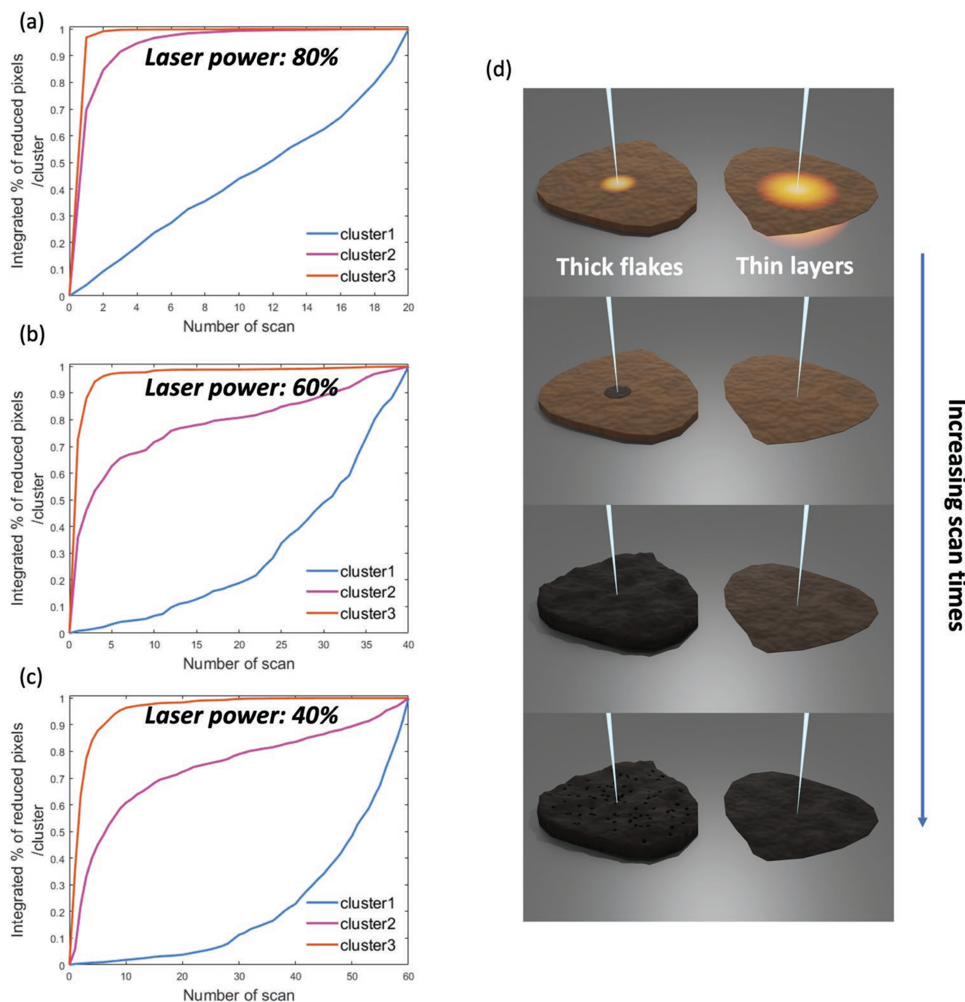

Figure 6. a–c) Integrated proportion of pixels that have reached or passed their peak degree of reduction, as a function of increasing number of laser scans for each cluster at 80%, 60%, and 40% laser power. d) Schematic diagram showing the difference in heat glow upon laser irradiation and the reduction mechanism of thick flakes and thin layers.

intensity distributions together demonstrate the distinct transformation processes of the two flakes. The intensity distribution histograms show a stable peak originating from the bare background glass substrate remains stable at 0.971 ± 0.003 transmission. For the thick graphite oxide flake (average thickness ≈25 nm, cluster 3), the initial GO material showed a transmission peak at a normalised intensity ≈0.5 (**Figure 7**). Initiation of local reduction is first observed from the micrographs after 3 scans (Figure 7a,b), where the original peak corresponding to GO splits into two peaks: the new one with lower intensity ≈0.3 indicates the presence of LrGO. As the reduced area increases (Figure 7b-d), this LrGO peak in the histogram grows, at the expense of the original GO peak. Eventually, after 9 scans, the flake is fully reduced; the images and histogram then remain stable until around scan 52 (Figure 7d–g), until a new peak in the histogram appears at 0.4, associated with the visual appearance of pores on the flake, attributed to ablation (Figure 7g–i). Reflection-mode monitoring confirmed the change of surface morphology during the reduction sequences (Figure S7, Supporting Information), including the rough surface of LrGO and the ablated structure (at scan 57 and 62) related to the thermally mediated process. Direct visualization of thick flake reduction is available with correlative movies constructed by sequential high-resolution transmission and reflection images (Video S3, Supporting Information). A typical thin GO flake (average thickness ≈5 nm, cluster 1) in the selected region showed two initial histogram peaks corresponding to the GO layers (major peak) and the substrate (Figure S8, Supporting Information). In contrast, to the thick flake, the GO peak shifts gradually as a single mode toward lower intensity with increasing laser scan number. No damage to the flake was observed. In summary, this high-resolution study of individual representative flakes is consistent with the mechanisms proposed in Section 2.2 in the large area, multi flake survey.

2.4. Microstructures of LrGO

In order to image the LrGO microstructure at higher resolution, using SEM, equivalent GO films were deposited on conductive doped silicon substrates. The microstructural differences between GO and LrGO are easily visualized in SEM,

 © 2023 The Authors. Advanced Functional Materials published by Wiley-VCH GmbH

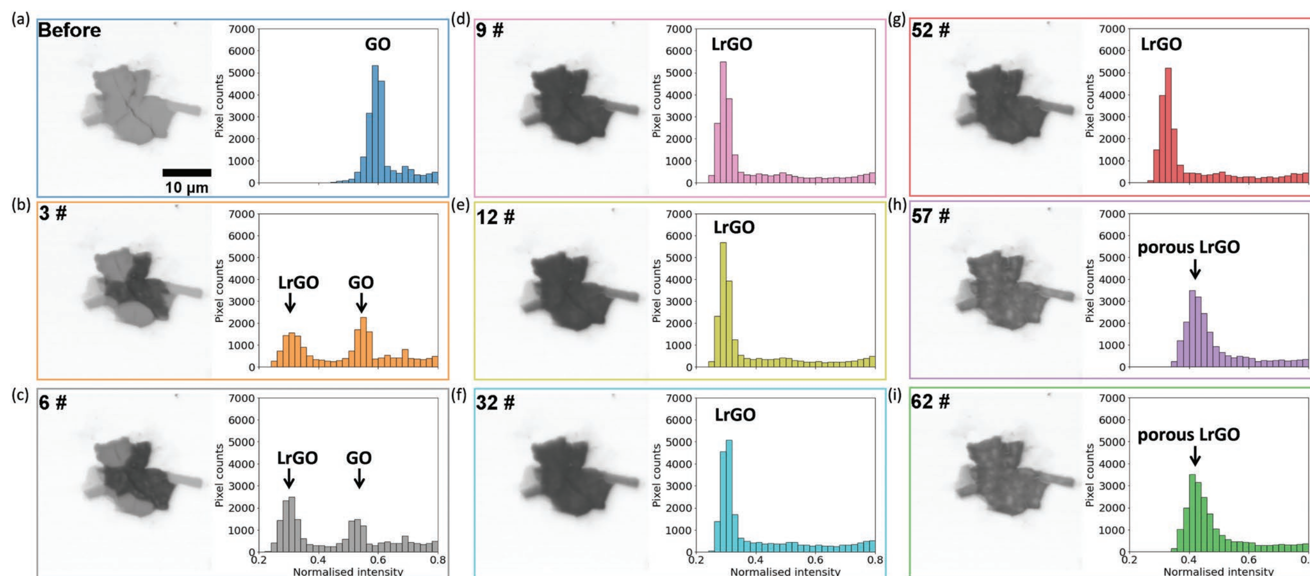

Figure 7. High-magnification (with the 50X/NA0.95 objective) transmission-mode monitoring of a thick GO flake (cluster 3) during the reduction process (laser intensity: 40%): a) Before reduction. b–i) After 3, 6, 9, 12, 32, 52, 57, and 62 laser scans. For each subfigure, the left image shows the transmission optical micrograph of the flake obtained with the 405 nm laser, and the histogram beside the image shows the transmission intensity distribution. Histograms in the same column share the X axis labels.

due to the different work functions and conductivity. An example of large flake located on the edge of the laser exposed area (**Figure 8**b) shows a clear boundary, where both GO and LrGO are resolved with distinct contrast. High magnification SEM images show the loose and rough graphitic structure of LrGO, in contrast to the smooth pristine GO (Figure 8a,c). In many regions, the transition between GO and rGO is continuously defined even within a single flake (Figure 8a), although in some cases cracks appear, likely due to thermal stress caused by the confined laser irradiation (Figure 8c). Interestingly, in the continuous regions, although the transition between reduced and unreduced material remains sharp, on the order of a few tens of nanometers, the path of the interface fluctuates on a sub-micron scale, likely due to variations in thermal contact. In addition, both partially reduced flakes and porous, ablated graphitic flakes were observed (Figure 8d,e), corresponding to the processes identified from the optical transmission images. The partially reduced flakes correspond to the start of the local reduction process (Figure 7b,c); bright regions of LrGO (highlighted by arrows in Figure 8d) with high secondary electron yield indicate the initiation of flake reduction, in contrast to the unreduced regions with lower conductivity. Porous flakes (e.g., Figure 8e) correspond to the ablated rGO at later stages of the reduction (Figure 7h,i).

Building on this investigation of individual flake structures, laser reduction was explored on continuous, drop-cast, GO films (average thickness ≈20 nm), which are more relevant to practical application. Optical microscopy shows striking color

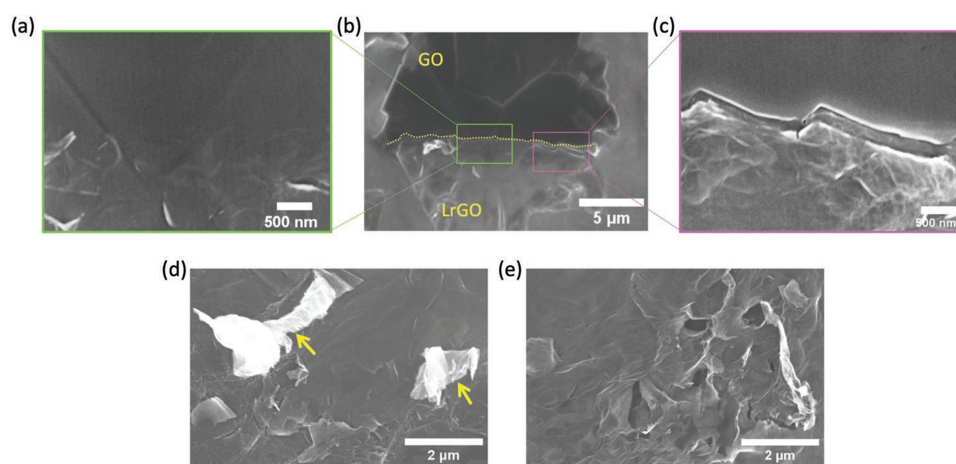

Figure 8. SEM images of GO and rGO at the boundary of the laser reduced area (laser intensity: 80%). a) High-magnification image of a continuous boundary region. b) SEM image of a flake on the edge of the laser irradiated region. c) High-magnification SEM image of a cracked boundary region. d) SEM image of a partially reduced flake. e) SEM image of a porous LrGO flake.

© 2023 The Authors. Advanced Functional Materials published by Wiley-VCH GmbH

16163028, 2023, 30, Downloaded from https://onlinelibrary.wiley.com/doi/10.1002/adfm.202300479 by Imperial College London, Wiley Online Library on [24/08/2023]. See the Terms and Conditions (https://onlinelibrary.wiley.com/terms-and-conditions) on Wiley Online Library for rules of use; OA articles are governed by the applicable Creative Commons License

16163028, 2023, 30, Downloaded from https://onlinelibrary.wiley.com/doi/10.1002/adfm.202300479 by Imperial College London, Wiley Online Library on [24/08/2023]. See the Terms and Conditions (https://onlinelibrary.wiley.com/terms-and-conditions) on Wiley Online Library for rules of use; OA articles are governed by the applicable Creative Commons License

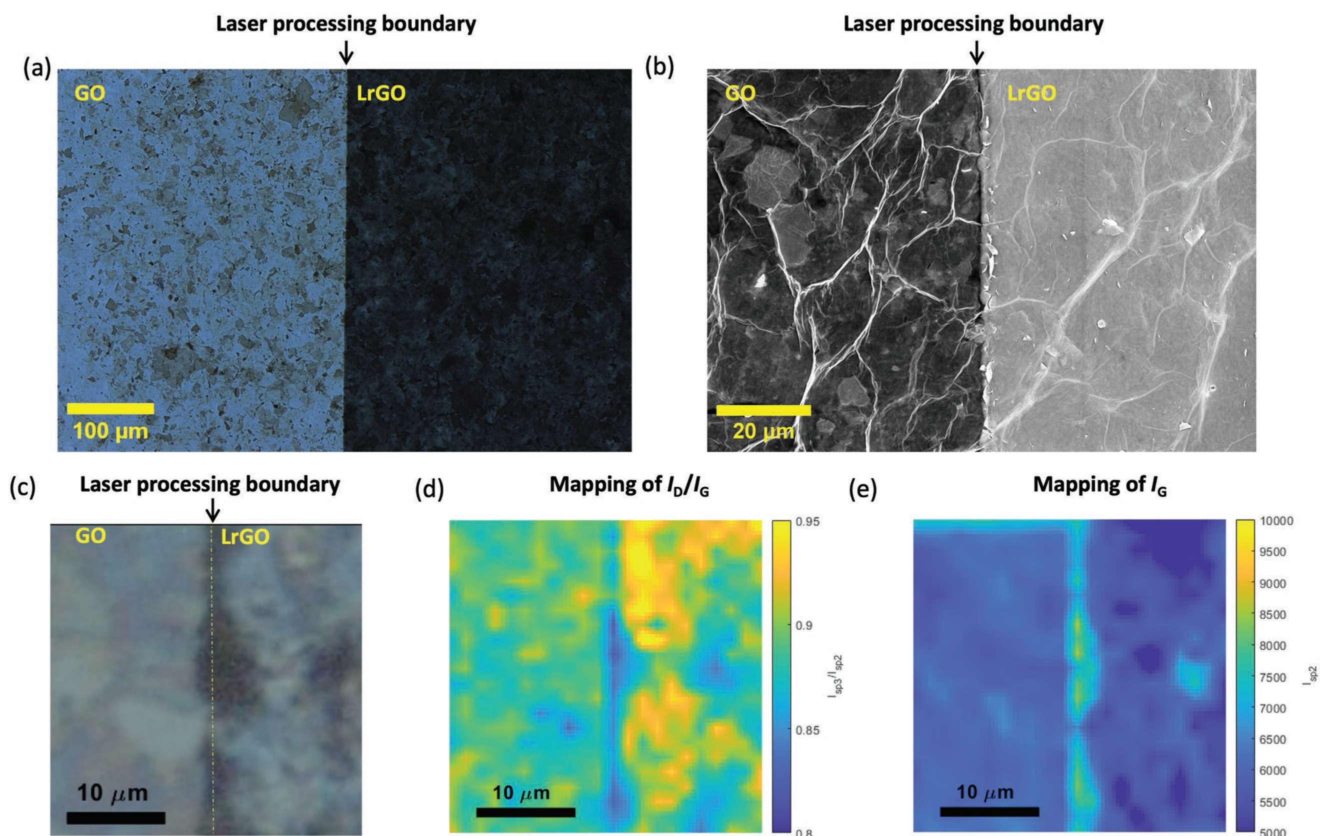

Figure 9. a) Single optical micrograph showing confined reduction (1 laser pass, laser intensity: 80%) on a drop-casted GO film. b) Single SEM image of a GO-LrGO transition region. c) Reflection image of a GO-LrGO region selected for Raman characterization. d) Raman mapping of I_D/I_G and e) I_G over the selected area.

differences between the GO and the much darker LrGO on a reduced film with single laser scan at 80% power (**Figure 9**a). A well-defined boundary is located between pristine GO film and LrGO film, as a result of the tightly-restricted laser irradiated region. In SEM, the thicker, dried film has a wrinkled surface structure, both before and after reduction, but again there is clear contrast between the GO and LrGO regions (Figure 9b); again, the LrGO is brighter, due to the increased secondary electron yield. The Raman spectra of GO and LrGO show the classic bands at 1594 cm^{-1} (G band) and 1347 cm^{-1} (D band) (Figure S9a, Supporting Information), associated with well-ordered and defective graphitic regions, respectively. GO and rGO have similar Raman spectra, due to the consistent graphitic area, although reduction generally increases the relative D band intensity due to the inverse I_D/I_G relation at high defect densities.[32] Raman mapping was applied at a GO-rGO transition region to characterize the structural differences further (Figure 9c). Mapping of the I_D/I_G ratio shows a sharp transition between GO and LrGO: an increase of I_D/I_G was observed for LrGO (Figure 9d), as expected.[32] Additionally, statistical Raman spectroscopy reveals a broader distribution of I_D/I_G, extending toward higher values (Figure S9b, Supporting Information). A decrease of I_G was observed across much of the LrGO, which may be caused by trapped gases evolving within thick flakes, scattering due to surface roughening or a density reduction associated with ablation (Figure 9e). Interestingly, there is a line of high I_g along the boundary between unprocessed and processed regions (Figure 9e), which correlates with apparently crystalline flakes dislodged from the film (Figure 9b); the lack of mechanical constraint and the opportunity for evolved gases to escape, may allow more effective regraphitization. Generally, the laser reduction of continuous GO films was found to be rapid and efficient, with significant microstructural alteration following even a single laser pass (633 ms for a reduced region of 159.7 µm × 159.7 µm), highlighting the practicality of the technique.

2.5. Manipulation of Reduction Patterns at Various Length Scales

Given the success of the sequential reduction process on both single flakes and macroscopic films, it was interesting to take advantage of flexibility offered by the confocal system to produce patterned GO over various length scales (**Figure 10**). Macroscale patterning was achieved with the image stitching module through sequential rastering of a pre-designed shape (Figure 10a,b). The example millimeter-scale pattern on a continuous GO film took less than 1.5 min to process, demonstrating the efficiency of the technique for device development. Precise micro-patterning of a dumbell shape (length ≈20 µm) on a single GO flake was realized through selective reduction

 © 2023 The Authors. Advanced Functional Materials published by Wiley-VCH GmbH

16163028, 2023, 30, Downloaded from https://onlinelibrary.wiley.com/doi/10.1002/adfm.202300479 by Imperial College London, Wiley Online Library on [24/08/2023]. See the Terms and Conditions (https://onlinelibrary.wiley.com/terms-and-conditions) on Wiley Online Library for rules of use; OA articles are governed by the applicable Creative Commons License

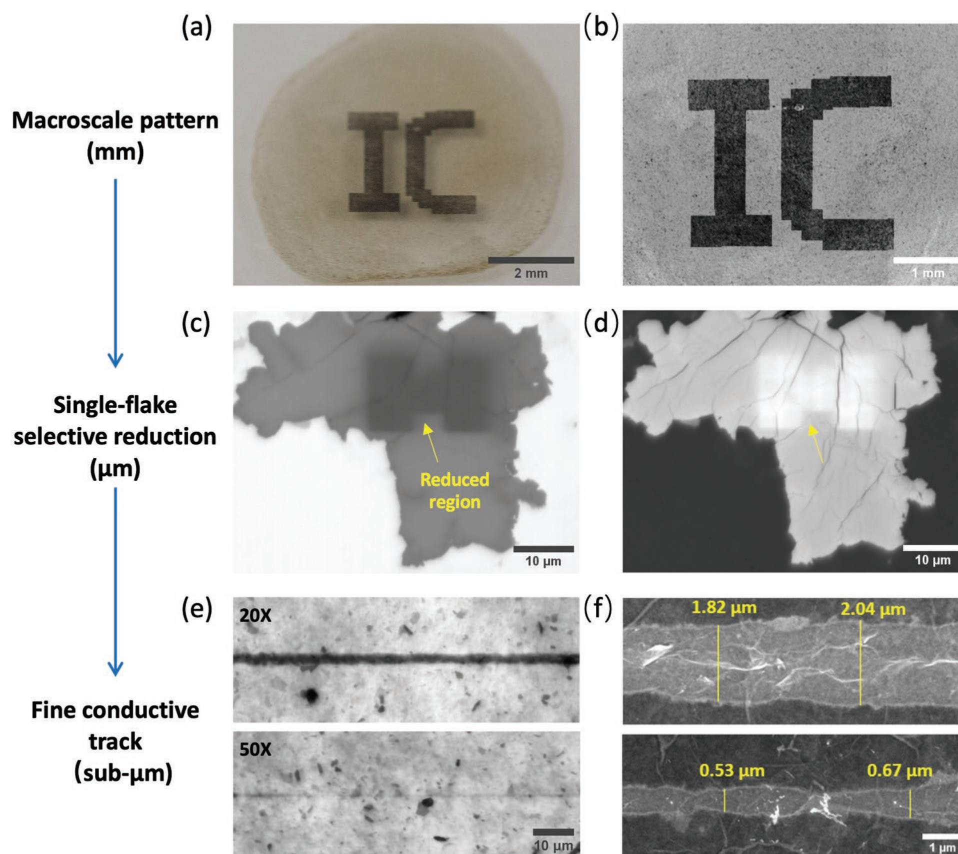

Figure 10. Demonstration of the multiscale reduction patterns. a) Digital image and b) stitched optical micrograph of the laser reduced macroscale pattern. c) Transmission-mode image and d) reflection-mode image of selective reduction (indicated by yellow arrows) on a single flake. e) Transmission-mode images of line profiles reduced with 20X and 50X objectives. f) SEM images of the lines reduced with 20X and 50X objectives.

using a 50X objective and a 40X digital zoom, and evidenced with both transmission and reflection images (Figure 10c,d). Finally, the line scan feature of CLSM allows for convenient fabrication of fine rGO tracks, the resolution of which can be controlled by varying the objective lens (Figure 10e). Using a 50X objective, tracks of LrGO were prepared with sub-micrometer linewidths, close to the wavelength of the laser applied (SEM, Figure 10f). Confocal techniques generally offer higher resolution compared to conventional microscope illumination due to the pointwise illumination optics,[33] as well as, here, the shorter wavelength, UV laser applied. This resolution advantage is exploited, in this study, to deliver sub-micron patterning, using a low power laser. The intrinsically enhanced lateral resolution of confocal microscopy is thus useful for not only high-quality imaging, but also precise laser processing of materials. Previous examples of high resolution laser patterning of GO have all relied on ultrashort wavelength or pulse width, expensive, pulsed systems.[12a,34]

The highly controllable and broad range of reduction patterns, from millimeter to submicrometer scale, demonstrates the efficiency of laser reduction within an integrated confocal microscope system. While photothermal reduction is typically considered poorly controlled in comparison with photochemical reduction, it is shown that fine control can be realized based on prior knowledge of the thermally mediated reduction process. The ability to perform efficient patterning with a low-cost continuous wave laser makes the proposed approach valuable for facile fabrication of GO and rGO based flexible electronics where localized processing is required.

To further demonstrate the general applicability of the technique, the surface morphology and electrical performance of LrGO was studied on spray-coated films. Spray coating is an important technique for scalable deposition of uniform GO films over larger areas and was applied here to demonstrate controlled reduction on thicker continuous GO films (average thickness ≈42 nm). RGO strips (1.8 mm × 7.8 mm) were fabricated with the 488 nm laser (80% power) on a uniformly deposited GO film, for electrical measurements (Figure S10a–c, Supporting Information). As observed for the drop-cast films (Figure 9), differences in surface texture are visible in the confocal reflection images (Figure S10d–g, Supporting Information), where the LrGO strips show a rough and fragmented surface structure. After 1 laser scan (80% power), the film was reduced, with an increase in roughness increased from 40.1 to 83.5 nm, due to laser-induced expansion. Increasing scan times lead to gradual decrease of film roughness due to laser ablation. At this power, 1 scan was sufficient for the LrGO to show significant electrical conductivity (2.5 kOhm sq^{-1}) in contrast to the pristine, insulating GO, with no significant further increase after subsequent cycles (See Figure S10, Supporting

© 2023 The Authors. Advanced Functional Materials published by Wiley-VCH GmbH

16163028, 2023, 30, Downloaded from https://onlinelibrary.wiley.com/doi/10.1002/adfm.202300479 by Imperial College London, Wiley Online Library on [24/08/2023]. See the Terms and Conditions (https://onlinelibrary.wiley.com/terms-and-conditions) on Wiley Online Library for rules of use; OA articles are governed by the applicable Creative Commons License

Information). The electrical performance of LrGO films fabricated is comparable with that reported for thermally and chemically reduced GO,[35] and matches the conductivity of recently reported LrGO conductors of similar thicknesses (fabricated with a high power pulsed laser).[13c] Since the laser reduction technique enables the fabrication of both large-scale patterns and thin lines of LrGO, a “patch and line” structure was designed to evaluate the conductivity of sub-micron tracks (Figure S11, Supporting Information). To measure the resistance at a fine scale, a micro two-point probe station was integrated with a digital microscope. The absolute patch resistance (20 kOhm) measured using the two-point probe was significantly lower than the line resistance (5 MOhm), so the contact resistance for the line measurement can be considered to be negligible. The conductivity of the line was estimated to be 1.4×10^3 S m^{-1} (resistivity: 6.9×10^{-4} Ohm m), while the large-scale conductivity, measured using a four-point probe, was $\approx 7.1 \times 10^3$ S m^{-1} (resistivity: 1.4×10^{-4} Ohm m). The conductivity values are consistent, given the uncertainty in the line dimensions, and the expected variations in homogeneity and inter-flake contact in a line patterned with similar width to the constituent flakes. The ability to fabricate the high-resolution conductive “patch and line” structure demonstrates the potential of the laser reduction technique for applications in microelectronics or other devices.

Increasing the number of scans had little effect on the conductivity presumably as ablation was compensated by the conductivity of underlying reduced layers (Figure S10, Supporting Information). However, the ability to perform film thinning while maintaining high electrical conductivity is not only promising for fabricating transparent rGO conductors, but also provides the possibility to pattern microscale architectures in three dimensions on GO films (Figure S12, Supporting Information). A block-structured inverse pyramid was patterned by varying scan times (1, 5, 10 scans), and the stepwise height differences can be observed from the surface topology map, where the center of the pyramid shows a very smooth surface after 10 scans. The high reproducibility and controllability of laser processing films illustrated across the various coating methods show that the technique is useful for reduction, thinning, and versatile patterning on various scales and dimensions.

3. Conclusion

In summary, we have investigated correlative characterization and in situ laser reduction of GO with CLSM. CLSM provides rapid and large-area characterization of GO through high-quality transmission, reflection, and fluorescence imaging. Multi-modal imaging and real-time monitoring allow for the direct observation and understanding of reduction processes, and their progress, on the scale of both single flakes and across large statistical survey areas. Quantitative analyses of the degree of reduction reveal a thermally-mediated reduction mechanism with strong flake-thickness dependence. The locus of the reduction is readily controlled across multiple length scales, from the millimeter range to submicron, using the built-in continuous-wave laser, operating at a low power (< 5 mW). A very high, wavelength-limited resolution (530 nm) was achieved, bypassing the usual low-resolution limitations of photothermal processing. This level of fine reduction has only been reported previously using high-cost pulsed laser sources.[12] The quality of the LrGO tracks is confirmed by their high conductivity (1.4×10^3 S m^{-1}). The performance could be further optimized with refinement of the feedstock coating and laser conditions and potentially applied to mechanically flexible substrates. In addition, the localized, laser-induced ablation processes can be used to sculpt microscale 3D architectures, which can again by monitored in situ using the topographic capability of CLSM. This in situ fabrication-characterization approach may be extended to other graphene precursors converted by laser processing in the future.[36] Overall, the simultaneous characterization and precise in situ reduction of GO with a single instrument demonstrates the potential of CLSM for locating, inspecting, and processing graphene-based materials and devices.

4. Experimental Section

Preparation of GO Films: As received GO water dispersion (Graphenea Inc., 4 mg ml^{-1}) was sonicated and diluted into various concentrations for film coating. Glass slides (VWR Inc.) and silicon wafers (TAAB Inc.) were cut, cleaned with isopropanol in an ultrasonic bath, then pretreated with oxygen plasma for 5 min under a plasma power of 70 W immediately before spin-coating dilute layers of GO flakes for mechanistic studies. GO solutions (200 µl) with two different concentrations (4 mg ml^{-1}, 40 µg ml^{-1}) were first dropped then spin coated onto substrates at a speed of 2000 rpm and dried at 70 °C on a hot plate. For film patterning, graphene oxide films were prepared by drop casting GO solutions (200 µl) with a concentration of 0.4 mg ml^{-1} onto heated substrates (70 °C). Spray coating was also applied to prepare continuous GO films. 1 ml of 0.4 mg ml^{-1} GO solution were continuously sprayed onto glass substrates by a handheld artist’s airbrush with a nozzle diameter of 250 µm.

Laser Processing and Monitoring of the Reduction Process: A Zeiss LSM 800 laser confocal scanning microscope was applied for in situ reduction and characterization of GO films. This compact confocal system employs diode lasers (405, 488, 561, and 640 nm) for excitation with a maximum laser energy of 5 mW; only the 405 nm was used for confocal reflection imaging. Reflection and fluorescence signals were captured with Multialkali photomultiplier tubes (PMT). Transmission images were collected with an electronically switchable illumination and detection (ESID) module. Various objective lens (5X/NA 0.2, 10X/NA 0.25, 10X/NA 0.4, 20X/NA 0.7, 50X/NA 0.6, 50X/NA 0.95) were fitted on the system. Together with a continuous adjustable scanning zoom (0.5X to 40X), the laser focused area can be changed flexibly from 3.2 µm × 3.2 µm to 2.56 mm × 2.56 mm. Multiple-pass imaging was applied with a high-numerical aperture objective (20X/NA 0.7), under ambient conditions, for monitoring the reduction process. The first pass applied a strong 488 nm laser power (40%–80%) to induce laser reduction of the GO films, while the photoluminescence signal was simultaneously detected in the range of 565–700 nm. In the second pass, a relatively weak 405 nm laser power (< 5%) was used to capture a transmission image of the reduced area. Periodic switching between the two passes was achieved through automatic hardware changes. A time lapse of 100 ms was set between each cycle of imaging. Confocal reflection images were taken with the 405 nm laser (0.7% power) before and after laser processing for comparisons of the surface structures. Widefield transmission optical micrographs were obtained with visible light to visualize the laser-reduced region. The reduction behavior of single GO flakes was observed with the 50X/NA 0.95 objective.

Image Processing: Unsupervised Clustering and Quantification of Reduction Degree: Quantification of transmission images was

© 2023 The Authors. Advanced Functional Materials published by Wiley-VCH GmbH

16163028, 2023, 30, Downloaded from https://onlinelibrary.wiley.com/doi/10.1002/adfm.202300479 by Imperial College London, Wiley Online Library on [24/08/2023]. See the Terms and Conditions (https://onlinelibrary.wiley.com/terms-and-conditions) on Wiley Online Library for rules of use; OA articles are governed by the applicable Creative Commons License

performed on selected regions to enhance visualization of the laser reduction process (Figure S1, Supporting Information). Image analysis was performed in Matlab with self-written scripts. The initial image (transmission image of GO films taken before laser reduction) was first thresholded to separate areas containing GO flakes from those without. The average intensity value of the area without GO flakes was determined as the incident intensity (I_0). First, pixel absorbance (A_{pixel}) was calculated over the image as:

$$A_{\text{pixel}} = -log_{10}\left(I_{\text{pixel}}/I_0\right) \tag{1}$$

Here, I_{pixel} refers to the light intensity of each pixel. A corresponding absorbance image stack was generated, which was converted from transmission micrographs taken during the reduction process. The maximum absorbance of each pixel was calculated from the image stack and recorded as the absorbance of rGO (A_{rGO}). The absorbance of GO (A_{GO}) was taken from that of the initial image. To track the reduction process temporally, a relative conversion degree (from GO to rGO) was calculated for each pixel:

$$\text{Conversion degree} = \left(A_{\text{pixel}} - A_{\text{GO}}\right)/\left(A_{\text{rGO}} - A_{\text{GO}}\right) \tag{2}$$

Conversion maps and videos were generated recording the pixel conversion corresponding to different stages of reduction.

The GO flakes were assigned to different phenomenological clusters, according to their response to laser processing, using an unsupervised *K*-means algorithm applied to the transmission images, implemented from the Scikit-learn library incorporated in Python. Raw transmission images were clustered into 4 categories, defined as: cluster 0 (substrates), cluster 1 (thin layers), cluster 2 (medium layers), and cluster 3 (thick flakes). Labelled cluster images and binary mask images of each cluster were exported at the end of the clustering module. The binary masks were then used to separate the clusters in the conversion maps and further statistical analysis was carried out in Matlab.

Evaluation of Film Properties: Roughness Analysis: 3D morphologies of LrGO films were characterized through surface mapping and roughness analysis with the LSM 800 confocal system. 3D stacks of the film surface were first obtained in confocal reflection mode (405 nm laser, 3.5% power), preprocessed in Zen Blue 2.6 and then analyzed in the ConfoMap software to generate pseudo-color 2D and 3D surface maps. Roughness analysis of films was performed using the 50X/NA 0.95 objective and a digital zoom of 0.6 in the *XY* range of 212.97 µm × 212.97 µm according to ISO 25178. A high-pass filter cut-off of 80 µm and a low-pass filter cut-off of 0.5 µm were applied for roughness analysis.

Characterization of LrGO Film: Microstructural characterization of laser reduced GO flakes and films was performed on a Zeiss Auriga field emission scanning electron microscope in the InLens imaging mode with an accelerating voltage of 5 kV at various magnifications. Equivalent samples reduced on conductive silicon substrates were prepared for SEM imaging. GO flake thickness was measured using an Asylum MFP-3D atomic force microscope, operating in tapping mode. The height profiles of GO flakes were analyzed using Gwyddion software, with image pre-processing steps including plane and scar correction prior to analysis. Raman characterization was performed using a ReniShaw Raman microscope with a 532 nm excitation laser (5% power), an exposure time of 10 s for each point and 1800 l mm^{-1} grating. Raman mapping over a selected region (31.5 µm × 31.5 µm) around the boundary of the laser exposed area was carried out at a step size of 2.5 µm. Large-area (3 mm × 3 mm) absorbance and reflectance spectra of GO films (spin-coated, 4 mg ml^{-1}) were obtained with a Shimadzu UV2600 integrating sphere spectrophotometer in the range of 300–800 nm. The fluorescence spectrum of GO films was obtained at the excitation wavelength of 488 nm using the spectral imaging function on the confocal microscope.

Electrical Resistance Measurements: The sheet resistance of GO and LrGO films were measured with a four-point probe connected to a Keysight 34410A Digital Multimeter data logger. The four-point probe geometry eliminates the effect of contact resistance, where ΔV represents the voltage change between the two inner probes, I is current flowing through the two outer probes. This method is often used to measure infinite 2D sheets, where the current is considered to flow cylindrically from the probes and the bulk resistivity can be determined from:[37]

$$\rho_{4-\text{p}} = \frac{\pi t}{\ln 2}\frac{\Delta V}{I} \tag{3}$$

in which t is the film thickness. The sheet resistance is defined as:

$$R_s = \frac{\rho_{4-p}}{t} \tag{4}$$

For each laser condition, resistance measurements were performed on the fabricated rGO strips (fabricated with dimensions 1.8 mm × 7.8 mm) at 8 different regions; the average sheet resistance is displayed in the corresponding confocal reflection image.

The electrical properties of conductive tracks were measured using a two-point probe station (T20-10, Lambda Inc) connected to a Lambda 1908P Digital Multimeter. The two-point probes (diameter: ≈1 µm) were carefully positioned on the contact patches patterned at the ends of LrGO lines (see Figure S11a, Supporting Information) using a Dino-lite digital microscope. In a typical two-point probe measurement, the bulk resistivity is given by:

$$\rho = \frac{\Delta VA}{I\,L} \tag{5}$$

Here, ΔV is the voltage drop across the sample, I is the current flowing through, A is the cross sectional area of the specimen and L is the length of the sample track. The two-point probe method is generally only considered suitable for measurement of specimens with relatively high resistance,[38] to ensure that contact resistance is not significant; this assumption was validated for the designed "patch and line" structure, as outlined above.

Supporting Information

Supporting Information is available from the Wiley Online Library or from the author.

Acknowledgements

The authors would like to acknowledge the support of Henry Royce Institute at Imperial College London for the use of confocal microscope, Chengning Yao for assistance with the two-point probe conductivity measurements, and Alexander Ford for helpful comments on the manuscript. Y.L. is grateful for the China Scholarship Council (CSC) and Imperial College London for funding support. M.S. would like to acknowledge the EU Graphene Flagship under Horizon 2020 Research and Innovation Programme grant agreement no. 881603 – GrapheneCore3.

Conflict of Interest

The authors declare no conflict of interest.

Data Availability Statement

The data that support the findings of this study are available from the corresponding author upon reasonable request.

© 2023 The Authors. Advanced Functional Materials published by Wiley-VCH GmbH

Keywords

confocal microscopy, graphene oxide, laser reduction, patterning

Received: January 12, 2023
Revised: March 14, 2023
Published online: April 25, 2023

[1] O. C. Compton, S. T. Nguyen, *Small* **2010**, *6*, 711.

[2] a) M. Sedki, P. S. Mirabedini, K. Nakama, G. Stephens, M. Groves, I. Lee, M. R. Neupane, A. Mulchandani, *Carbon* **2022**, *186*, 437; b) G. Eda, G. Fanchini, M. Chhowalla, *Nat. Nanotechnol.* **2008**, *3*, 270; c) H. Yamaguchi, G. Eda, C. Mattevi, H. Kim, M. Chhowalla, *ACS Nano* **2010**, *4*, 524.

[3] S. Pei, H. M. Cheng, *Carbon* **2012**, *50*, 3210.

[4] a) D. Voiry, J. Yang, J. Kupferberg, R. Fullon, C. Lee, H. Y. Jeong, H. S. Shin, M. J. S. Chhowalla, *Science* **2016**, *353*, 1413; b) D. R. Dreyer, S. Park, C. W. Bielawski, R. S. Ruoff, *Chem. Soc. Rev.* **2010**, *39*, 228; c) C. K. Chua, M. Pumera, *Chem. Soc. Rev.* **2014**, *43*, 291.

[5] a) F. Alotaibi, T. T. Tung, M. J. Nine, S. Kabiri, M. Moussa, D. N. Tran, D. Losic, *Carbon* **2018**, *127*, 113; b) M. F. El Kady, V. Strong, S. Dubin, R. B. J. S. Kaner, *Science* **2012**, *335*, 1326; c) J. Zhang, P. Hu, R. Zhang, X. Wang, B. Yang, W. Cao, Y. Li, X. He, Z. Wang, W. O'Neill, *J. Mater. Chem.* **2012**, *22*, 714.

[6] a) F. Li, M. Xue, X. Ma, M. Zhang, T. Cao, *Anal. Chem.* **2011**, *83*, 6426; b) J. Y. Hong, J. Jang, *J. Mater. Chem.* **2012**, *22*, 8179; c) Z. Wei, D. Wang, S. Kim, S. Y. Kim, Y. Hu, M. K. Yakes, A. R. Laracuente, Z. Dai, S. R. Marder, C. Berger, *Science* **2010**, *328*, 1373; d) J. M. Mativetsky, E. Treossi, E. Orgiu, M. Melucci, G. P. Veronese, P. Samorì, V. Palermo, *J. Am. Chem. Soc.* **2010**, *132*, 14130; e) P. H. Wöbkenberg, G. Eda, D. S. Leem, J. C. De Mello, D. D. Bradley, M. Chhowalla, T. D. Anthopoulos, *Adv. Mater.* **2011**, *23*, 1558.

[7] a) W. Gao, N. Singh, L. Song, Z. Liu, A. L. M. Reddy, L. Ci, R. Vajtai, Q. Zhang, B. Wei, P. M. J. N. n. Ajayan, *Nat. Nanotechnol.* **2011**, *6*, 496; b) H. Tian, H. Y. Chen, T. L. Ren, C. Li, Q. T. Xue, M. A. Mohammad, C. Wu, Y. Yang, H. S. P. Wong, *Nano Lett.* **2014**, *14*, 3214; c) L. Guo, H. B. Jiang, R. Q. Shao, Y. L. Zhang, S. Y. Xie, J. N. Wang, X. B. Li, F. Jiang, Q. D. Chen, T. Zhang, *Carbon* **2012**, *50*, 1667.

[8] a) R. You, Y. Q. Liu, Y. L. Hao, D. D. Han, Y. L. Zhang, Z. You, *Adv. Mater.* **2020**, *32*, 1901981; b) Z. Wan, E. W. Streed, M. Lobino, S. Wang, R. T. Sang, I. S. Cole, D. V. Thiel, Q. Li, *Adv. Mater. Technol.* **2018**, *3*, 1700315.

[9] a) Z. Wan, S. Wang, B. Haylock, J. Kaur, P. Tanner, D. Thiel, R. Sang, I. S. Cole, X. Li, M. Lobino, Q. Li, *Carbon* **2019**, *141*, 83; b) N. Q. Deng, H. Tian, Z. Y. Ju, H. M. Zhao, C. Li, M. A. Mohammad, L. Q. Tao, Y. Pang, X. F. Wang, T. Y. Zhang, Y. Yang, T. L. Ren, *Carbon* **2016**, *109*, 173.

[10] T. X. Tran, H. Choi, C. H. Che, J. H. Sul, I. G. Kim, S. M. Lee, J. H. Kim, J. B. In, *ACS Appl. Mater. Interfaces* **2018**, *10*, 39777.

[11] a) D. A. Sokolov, C. M. Rouleau, D. B. Geohegan, T. M. Orlando, *Carbon* **2013**, *53*, 81; b) Z. Qiao, C. Qin, W. He, Y. Gong, G. Zhang, R. Chen, Y. Gao, L. Xiao, S. Jia, *Opt. Express* **2017**, *25*, 31025; c) E. Orabona, A. Ambrosio, A. Longo, G. Carotenuto, L. Nicolais, P. J. O. l. Maddalena, *Opt. Lett.* **2014**, *39*, 4263.

[12] Z. B. Liu, L. Li, Y. F. Xu, J. J. Liang, X. Zhao, S. Q. Chen, Y. S. Chen, J. G. Tian, *J. Opt.* **2011**, *13*, 085601.

[13] a) D. A. Sokolov, K. R. Shepperd, T. M. Orlando, *J. Phys. Chem. Lett.* **2010**, *1*, 2633; b) V. Strong, S. Dubin, M. F. El Kady, A. Lech, Y. Wang, B. H. Weiller, R. B. Kaner, *ACS Nano* **2012**, *6*, 1395; c) A. L. Sanati, A. Chambel, P. A. Lopes, T. Nikitin, R. Fausto, M. Tavakoli, *Adv. Mater. Interfaces* **2022**, *9*, 2102343.

[14] a) M. Soni, P. Kumar, J. Pandey, S. K. Sharma, A. Soni, *Carbon* **2018**, *128*, 172; b) R. Arul, R. N. Oosterbeek, J. Robertson, G. Xu, J. Jin, M. C. Simpson, *Carbon* **2016**, *99*, 423.

[15] D. A. Sokolov, Y. V. Morozov, M. P. McDonald, F. Vietmeyer, J. H. Hodak, M. Kuno, *Nano Lett.* **2014**, *14*, 3172.

[16] M. P. McDonald, A. Eltom, F. Vietmeyer, J. Thapa, Y. V. Morozov, D. A. Sokolov, J. H. Hodak, K. Vinodgopal, P. V. Kamat, M. Kuno, *Nano Lett.* **2013**, *13*, 5777.

[17] D. J. Kim, C. W. Lee, Y. Suh, H. Jeong, I. Jo, J. Moon, M. Park, Y. S. Woo, B. H. Hong, *2D Mater.* **2020**, *7*, 045014.

[18] V. Panchal, Y. Yang, G. Cheng, J. Hu, M. Kruskopf, C. I. Liu, A. F. Rigosi, C. Melios, A. R. Hight Walker, D. B. Newell, O. Kazakova, R. E. Elmquist, *Commun. Phys.* **2018**, *1*, 83.

[19] a) J. Shang, L. Ma, J. Li, W. Ai, T. Yu, G. G. Gurzadyan, *Sci. Rep.* **2012**, *2*, 792; b) B. R. Coleman, T. Knight, V. Gies, Z. J. Jakubek, S. Zou, *ACS Appl. Mater. Interfaces* **2017**, *9*, 28911; c) A. T. Dideikin, A. Y. Vul, *Front. Phys.* **2019**, *6*, 149.

[20] I. Jung, M. Vaupel, M. Pelton, R. Piner, D. A. Dikin, S. Stankovich, J. An, R. S. Ruoff, *J. Phys. Chem. C* **2008**, *112*, 8499.

[21] R. H. Webb, *Rep. Prog. Phys.* **1996**, *59*, 427.

[22] J. Shang, L. Ma, J. Li, W. Ai, T. Yu, G. G. Gurzadyan, *Sci. Rep.* **2012**, *2*, 792.

[23] K. Fan, X. Chen, X. Liu, Y. Liu, W. Lai, Y. Chen, X. Liu, X. Wang, *Carbon* **2020**, *165*, 386.

[24] V. A. Smirnov, A. A. Arbuzov, Y. M. Shul'ga, S. A. Baskakov, V. M. Martynenko, V. E. Muradyan, E. I. Kresova, *High Energy Chem.* **2011**, *45*, 57.

[25] D. J. Joe, S. Kim, J. H. Park, D. Y. Park, H. E. Lee, T. H. Im, I. Choi, R. S. Ruoff, K. J. Lee, *Adv. Mater.* **2017**, *29*, 1606586.

[26] I. Jung, M. Pelton, R. Piner, D. A. Dikin, S. Stankovich, S. Watcharotone, M. Hausner, R. S. Ruoff, *Nano Lett.* **2007**, *7*, 3569.

[27] a) R. Cohn, E. Holm, *Integr. Mater. Manuf. Innovation* **2021**, *10*, 231; b) M. J. Abedin, T. Barua, M. Shaibani, M. Majumder, *Adv. Sci. (Weinh)* **2020**, *7*, 2001600.

[28] Y. Hwangbo, C. K. Lee, A. E. MagIsa, J. W. Jang, H. J. Lee, S. B. Lee, S. S. Kim, J. H. Kim, *Carbon* **2014**, *77*, 454.

[29] V. G. Plotnikov, V. A. Smirnov, M. V. Alfimov, Y. M. Shul'ga, *High Energy Chem.* **2011**, *45*, 411.

[30] a) Y. M. Shulga, V. Martynenko, V. Muradyan, S. Baskakov, V. Smirnov, G. Gutsev, *Chem. Phys. Lett.* **2010**, *498*, 287; b) J. N. Ma, J. W. Mao, D. D. Han, X. Y. Fu, Y. X. Wang, Y. L. Zhang, *Adv. Mater. Technol.* **2019**, *4*, 1900554.

[31] a) Y. Wang, N. Xu, D. Li, J. Zhu, *Adv. Funct. Mater.* **2017**, *27*, 1604134; b) A. Alofi, G. Srivastava, *Phys. Rev. B* **2013**, *87*, 115421.

[32] G. Eda, M. Chhowalla, *Adv. Mater.* **2010**, *22*, 2392.

[33] a) S. W. Paddock, *BioTechniques* **1999**, *27*, 992; b) T. Wilson, *Confocal Microscopy*, Academic Press, London **1990**.

[34] a) Y. Zhang, L. Guo, S. Wei, Y. He, H. Xia, Q. Chen, H. B. Sun, F. S. Xiao, *Nano Today* **2010**, *5*, 15; b) S. Prezioso, F. Perrozzi, M. Donarelli, F. Bisti, S. Santucci, L. Palladino, M. Nardone, E. Treossi, V. Palermo, L. Ottaviano, *Langmuir* **2012**, *28*, 5489.

[35] a) X. Wang, L. Zhi, K. Müllen, *Nano Lett.* **2008**, *8*, 323; b) B. Zhao, P. Liu, Y. Jiang, D. Pan, H. Tao, J. Song, T. Fang, W. Xu, *J. Power Sources* **2012**, *198*, 423; c) V. H. Pham, T. V. Cuong, S. H. Hur, E. W. Shin, J. S. Kim, J. S. Chung, E. J. Kim, *Carbon* **2010**, *48*, 1945; d) D. W. Lee, T.-K. Hong, D. Kang, J. Lee, M. Heo, J. Y. Kim, B.-S. Kim, H. S. Shin, *J. Mater. Chem.* **2011**, *21*, 3438.

[36] a) M. G. Stanford, C. Zhang, J. D. Fowlkes, A. Hoffman, I. N. Ivanov, P. D. Rack, J. M. Tour, *ACS Appl. Mater. Interfaces* **2020**, *12*, 10902; b) W. H. Lee, J. W. Suk, H. Chou, J. Lee, Y. Hao, Y. Wu, R. Piner, D. Akinwande, K. S. Kim, R. S. Ruoff, *Nano Lett.* **2012**, *12*, 2374.

[37] I. Miccoli, F. Edler, H. Pfnür, C. Tegenkamp, *J. Phys.: Condens. Matter* **2015**, *27*, 223201.

[38] Y. Singh, *Int. J. Mod. Phys.: Conf. Ser.* **2013**, *22*, 746.

© 2023 The Authors. Advanced Functional Materials published by Wiley-VCH GmbH

16163028, 2023, 30, Downloaded from https://onlinelibrary.wiley.com/doi/10.1002/adfm.202300479 by Imperial College London, Wiley Online Library on [24/08/2023]. See the Terms and Conditions (https://onlinelibrary.wiley.com/terms-and-conditions) on Wiley Online Library for rules of use; OA articles are governed by the applicable Creative Commons License